

The Impact of the Bulk Structure on Surface Dynamics of Complex Mo-V-based Oxide Catalysts

Annette Trunschke, Johannes Noack, Sergej I. Trojanov, Frank Girgsdies, Thomas Lunkenbein, Verena Pfeifer, Michael Hävecker, Pierre Kube, Christoph Sprung, Frank Rosowski, and Robert Schloegl

ACS Catal., **Just Accepted Manuscript** • DOI: 10.1021/acscatal.7b00130 • Publication Date (Web): 21 Mar 2017

Downloaded from <http://pubs.acs.org> on March 25, 2017

Just Accepted

“Just Accepted” manuscripts have been peer-reviewed and accepted for publication. They are posted online prior to technical editing, formatting for publication and author proofing. The American Chemical Society provides “Just Accepted” as a free service to the research community to expedite the dissemination of scientific material as soon as possible after acceptance. “Just Accepted” manuscripts appear in full in PDF format accompanied by an HTML abstract. “Just Accepted” manuscripts have been fully peer reviewed, but should not be considered the official version of record. They are accessible to all readers and citable by the Digital Object Identifier (DOI®). “Just Accepted” is an optional service offered to authors. Therefore, the “Just Accepted” Web site may not include all articles that will be published in the journal. After a manuscript is technically edited and formatted, it will be removed from the “Just Accepted” Web site and published as an ASAP article. Note that technical editing may introduce minor changes to the manuscript text and/or graphics which could affect content, and all legal disclaimers and ethical guidelines that apply to the journal pertain. ACS cannot be held responsible for errors or consequences arising from the use of information contained in these “Just Accepted” manuscripts.

1
2
3
4
5
6
7 The Impact of the Bulk Structure on Surface Dynamics of Complex Mo-V-based
8
9
10 Oxide Catalysts
11
12

13 Annette Trunschke,^{1,*} Johannes Noack,^{1,2} Sergej Trojanov,³ Frank Girgsdies,¹

14 Thomas Lunkenbein,¹ Verena Pfeifer,^{1,4} Michael Hävecker,^{1,5} Pierre Kube,¹ Christoph Sprung,¹

15
16
17
18 Frank Rosowski,⁶ Robert Schlögl¹
19
20

21 ¹Department of Inorganic Chemistry, Fritz-Haber-Institut der Max-Planck-Gesellschaft,
22 Faradayweg 4-6, 14195, Berlin, Germany

23 ²UniCat-BASF Joint Lab, Technische Universität Berlin, Sekr. EW K 01, Hardenbergstraße 36,
24 10623 Berlin, Germany

25 ³Humboldt-Universität zu Berlin, Institut für Chemie, Brook-Taylor-Str. 2, 12489 Berlin,
26 Germany

27 ⁴Catalysis for Energy, Group EM-GKAT, Helmholtz-Zentrum Berlin für Materialien und
28 Energie GmbH, Elektronenspeicherring BESSY II, Albert-Einstein-Str. 15, 12489 Berlin,
29 Germany

30 ⁵Department of Heterogeneous Reactions, Max-Planck-Institut für Chemische
31 Energiekonversion, Stiftstr. 34-36, 45470 Mülheim a. d. Ruhr, Germany

32 ⁶BASF SE, Process Research and Chemical Engineering, Heterogeneous Catalysis, Carl-Bosch-
33 Straße 38, 67056, Ludwigshafen, Germany
34
35
36
37
38
39
40
41
42
43

44 Corresponding author: trunschke@fhi-berlin.mpg.de
45
46
47
48
49
50
51
52
53
54
55
56
57
58
59
60

ABSTRACT

Mixed oxides composed of the four metals Mo, V, Te, and Nb are known to be efficient catalysts in selective oxidation of lower alkanes. The outstanding catalytic performance of such mixed oxides is attributed to the presence of the so-called M1 crystal phase that contains all four elements in the metal positions of the structure. In the present work, a M1 phase composed only of Mo and V has been prepared by hydrothermal synthesis. High crystallinity was achieved by applying a synthesis temperature of 200°C. The phase-pure mixed MoV oxide was studied as catalyst in the oxidation of propane. In contrast to previous reports, the desirable oxidation product acrylic acid is formed over the Te-free M1 structure in significant amounts implying that Te is not necessarily required as a component of the active ensemble responsible for selective oxygen insertion. The MoV M1 oxide is, however, less selective compared to the M1 structure composed of the four metals Mo, V, Te, and Nb. The reason has been figured out by applying a combination of synchrotron-based single crystal structure analysis and near-ambient-pressure XPS. Determination of the crystal structure of MoV M1 oxide reveals partial occupation of sites in the hexagonal channels of the M1 structure by V, which are occupied by Te in MoVTeNb M1 oxide. Hydrolysis of the M-O bonds (M=V, Te) under reaction conditions leads to migration of the metal in the hexagonal channels to the surface. Accumulation of more than 50 at% V on the surface of the MoV M1 oxide most likely causes post-combustion of formed acrylic acid, while enrichment of Te at the surface of MoVTeNb M1 oxide results in dilution of surface V^{5+} species, and, consequently, in high selectivity.

KEYWORDS

selective oxidation, M1 structure, NAP-XPS, single crystal analysis, MoV, Te, propane, acrylic acid

INTRODUCTION

Mixed oxides are widely applied as catalysts in selective oxidation reactions and electrocatalysis.¹⁻⁸ Conceptual understanding of bulk mixed oxides on the molecular level is, however, limited due to the often very complex structural and surface chemistry of this materials class. Activity and selectivity are frequently attributed to the crystal structure and the exposure of specific surface facets. One example is the *ab* plane of the so-called “M1 phase” (ICSD 55097)⁹⁻¹⁰ of MoVTeNb oxide.¹¹⁻¹³ Crystalline MoVTeNb oxide exclusively composed of the M1 phase catalyzes the selective oxidation of propane to acrylic acid and shows high activity and selectivity, whereas isomorphous MoV oxide is unselective and transforms propane mainly into carbon oxides.¹⁴

Selectivity to acrylic acid has been attributed to the function of tellurium in catalytic ensembles at the catalyst surface.¹⁴ It has been postulated that Te is responsible for α -H abstraction of the chemisorbed propene molecule, once formed by oxidative dehydrogenation of propane at cooperating vanadium and molybdenum oxide sites.¹² The activation of the first C-H bond in the methylene group of the propane molecule is attributed to $V^{5+}=O$ surface species, while $O=Mo^{6+}=O$ sites contribute to propene formation by abstraction of the second hydrogen atom. The intermediate product propene may desorb and re-adsorb or migrate to $Te^{4+}-O$ sites responsible for the formation of a π -allylic intermediate by α -H abstraction. Subsequent oxygen insertion is again attributed to molybdenum dioxo sites. The entire mechanistic concept has been

1
2
3 postulated taking into account the chemical complexity of the MoVTeNb mixed oxide assuming
4 structural definition of the surface in terms of an ideal cut of the bulk crystal structure.¹²
5
6 Differences in metal site occupancy hence will have an impact on the chemical composition of
7
8 the active ensemble,¹⁵ and on catalytic activity.¹⁶ Clear experimental proof of this concept is still
9
10 missing. Alternatively an active function of Te=O in propane activation has been proposed.¹⁷
11
12 According to the so-called reduction-coupled oxo activation mechanism, the Te=O bond accepts
13
14 the proton from the propane molecule while the electron goes to adjacent reducible V or Mo
15
16 sites. The latter concept is in agreement with the experimentally observed enrichment of the
17
18 MoVTeNb oxide surface in tellurium and vanadium under reaction conditions of propane
19
20 oxidation.¹⁸⁻²⁰
21
22
23
24
25
26

27 The current work is aimed at probing the surface of MoV M1 oxide under working conditions
28
29 by synchrotron-based near-ambient-pressure X-ray photoelectron spectroscopy (NAP-XPS) to
30
31 shed light on the differences in the catalytic properties of MoV and MoVTeNb oxide in
32
33 oxidation of propane to acrylic acid. For this purpose, phase-pure MoV oxide composed of the
34
35 M1 structure has been prepared. The high crystallinity of the material permitted a synchrotron-
36
37 based single-crystal structure analysis. Our results clearly show an impact of the crystalline bulk
38
39 structure on surface composition and reactivity of Mo-based mixed oxides in selective oxidation
40
41 of propane. The experiments illustrate critical relations between solid-state and surface dynamics
42
43 in oxidation catalysis.
44
45
46
47
48
49

50 EXPERIMENTAL DETAILS

51
52

53 Highly crystalline MoVO_x catalyst composed of the M1 structure was synthesized by a
54
55 hydrothermal method and subsequent washing procedure. A specially built reactor (Premex
56
57
58
59
60

1
2
3 Reactor AG, Lengnau, Switzerland) from corrosion resistant Hastelloy C-22 (2.4602) was
4
5 utilized, which enables precise control of the reaction parameters. A mixture of 9.18 g
6
7 $(\text{NH}_4)_6\text{Mo}_7\text{O}_{24}\cdot 4\text{H}_2\text{O}$ (AHM, Merck, 52 mmol Mo) dissolved in 230 g water (Milli-Q, Merck)
8
9 and 3.30 g VO_2 (Acros Organics, 12.9 mmol V) dissolved in 30 g water was loaded into a
10
11 hydrothermal reactor at room temperature. The vessel was heated to 200°C at a rate of 1°C/min
12
13 and hold at this temperature for 17 h. The reaction mixture is stirred during the whole experiment
14
15 at a rate of 100 rpm. The recorded reaction parameters are presented in Fig. S1.
16
17
18

19
20 After cooling to room temperature, a black solid (3.4 g) was isolated by filtration (pore 5 glass
21
22 frit), washed twice with distilled water and dried at 80°C for 16 hours. To remove amorphous
23
24 components, 1 g of the powder was washed with 25 ml oxalic acid solution (0.25 M, Acros
25
26 Organics) at 60°C for 30 min under stirring. The solid was centrifuged (5000 rpm, 30 min),
27
28 washed twice with 25 ml water and dried at 80°C over night. About 0.66 g of the washed sample
29
30 was recovered. Thermal treatment before analysis and catalytic testing was done in flowing
31
32 argon (flow rate 100 ml/min) at 400°C (heating rate 10°C/min) for 2 h in a rotary tube furnace
33
34 (Xerion, Freiberg, Germany), (catalyst ID 18075).
35
36
37
38

39 Powder XRD measurements were performed on a STOE STADI P transmission diffractometer
40
41 equipped with a primary focusing germanium monochromator ($\text{Cu K}\alpha_1$ radiation) and DECTRIS
42
43 MYTHEN 1K position sensitive solid-state detector. The samples were mounted in the form of
44
45 small amounts of powder sandwiched between two layers of polyacetate film and fixed with a
46
47 small amount of X-ray amorphous grease. The powder pattern was analyzed using the TOPAS
48
49 software (version 5, Bruker AXS 2014) by whole powder pattern fitting. Initially, a Pawley fit
50
51 based on the M1 unit cell was used to judge the phase purity. After obtaining a crystal structure
52
53
54
55
56
57
58
59
60

1
2
3 model from single crystal synchrotron data, this model was used for a Rietveld fit of the powder
4 data. In both cases no residual reflections not attributable to the M1 structure were observed.
5
6

7
8 The crystal structure of MoV M1 oxide was analyzed by single crystal analysis applying
9 synchrotron radiation at the MX 14.2 beam-line at BESSY II of the HZB (Helmholtz-Zentrum,
10 Berlin. The crystal structure was refined with SHELXL-2014 (G. M. Sheldrick, 2014), using the
11 coordinates of Sadakane *et al.* as starting model.²¹ However, as the *z* value of the origin in space
12 group *Pba2* can be freely chosen, we shifted the average plane of equatorial oxygen atoms to *z* =
13 0.5. Initially, all framework metal atoms were refined as mixed Mo/V sites. Several sites, which
14 converged sufficiently close to full Mo occupancy, were subsequently treated as Mo only sites.
15 Before the finalization of the structure model, all metal sites were refined anisotropically, while
16 oxygen atoms had to be treated isotropically. Since the anisotropic displacement parameters for
17 M2 and M12 indicated possible site splitting, these sites were subsequently split and refined
18 isotropically. Some residual electron density peaks which were observed in the hexagonal and
19 heptagonal channels (apart from M12) were, judging from their distances to other atoms,
20 considered to represent either oxygen atoms associated with M12, water molecules, or
21 ammonium ions. In all cases, these were treated as oxygen atoms. Since the low electron density
22 and overlapping contact radii indicated only partial occupancy, the occupancy was refined while
23 the isotropic thermal parameter was arbitrarily fixed at 0.02 Å² to avoid strong parameter
24 correlations.
25
26
27
28
29
30
31
32
33
34
35
36
37
38
39
40
41
42
43
44
45
46

47 Scanning electron microscopy (SEM) images were recorded on Hitachi S-4800 scanning
48 electron microscope equipped with field emission gun (FEG) with an acceleration voltage of 1.5
49 kV. Prior to imaging, the samples were dispersed on a conductive carbon tape (plano). Elemental
50
51
52
53
54
55
56
57
58
59
60

1
2
3 analysis was obtained by using X-ray dispersive spectroscopy (EDX). The measurement was
4
5 carried out at 15 kV and sampled at an EDAX detector connected to the Hitachi S-4800.
6
7

8 Scanning transmission electron microscopy (STEM) was conducted on a double corrected
9
10 JEOL JEM-ARM200F equipped with a CEOS CESCOR and a CEOS CETCOR hexapole
11
12 aberration correctors for probe and image forming lenses, respectively. A cold FEG (CFEG) is
13
14 used for electron extraction. Images were recorded with an acceleration voltage of 200 kV
15
16 inserting a high angle annular dark field (HAADF) or annular bright field (ABF) detector after
17
18 the sample. The sample was prepared via cross sectioning the MoV M1 oxide crystals.
19
20
21

22 The surface area determination was carried out in a volumetric N₂ physisorption apparatus
23
24 (Autosorb-6-B, Quantachrome) at 77 K. The sample was degassed in dynamic vacuum at a
25
26 temperature of 150°C for 2 h prior to adsorption. The adsorption isotherm was measured in the
27
28 range $p/p_0 = 0.0-0.35$. The specific surface area was calculated according to the BET method in
29
30 the pressure range $p/p_0 = 0.05-0.35$ using 11 data points. Pore size distribution in the micropore
31
32 range was analyzed applying the method of Horvath and Kawazoe based on adsorption in the
33
34 pressure range $p/p_0 = 0.0-0.001$.²²
35
36
37
38

39 The gas-phase propane oxidation was carried out in fixed-bed tubular reactors in continuous
40
41 flow mode in a 10-fold parallel reactor unit (ILS, Germany) that has been described in detail
42
43 before.²³ Typically, 0.5 g of powdered catalyst was first binder-free pressed under 1.25 MPa,
44
45 crushed and sieved to a particle size of 150-200 μm . Then, 40 mg of the catalyst were loaded into
46
47 a tubular reactor with an inner diameter of 2 mm. The feed was composed of C₃H₈, O₂, H₂O, and
48
49 N₂ in a molar ratio of 3 : 6 : 20 : 71, and 3 : 6 : 40 : 5 vol%, respectively. The reaction was
50
51 carried out at 250 – 300°C. Gas analysis was performed by an online gas chromatograph (7890A,
52
53 Agilent). A combination of two capillary columns (Poraplot Q and Plot Molesieve) in connection
54
55
56
57
58
59
60

1
2
3 with a thermal conductivity detector is used to analyze the permanent gases. A combination of
4 two capillary columns (HP-FFAP and Poraplot Q) connected to a flame ionization detector is
5 used to analyze alkanes, olefins, and oxygenates. A carbon balance of $100 \pm 5\%$ was calculated.
6
7
8
9

10 In-situ XPS was performed at the synchrotron facility BESSY II of the HZB (Helmholtz-
11 Zentrum Berlin) using tunable, monochromatic radiation of the ISIS (Innovative Station for In-
12 Situ Spectroscopy) beam line. The spectra were collected in the presence of reactive gases at
13 elevated temperature using a near-ambient-pressure XPS (NAP-XPS) system described in detail
14 elsewhere.²⁴ Briefly, 10.7 mg of MoV oxide powder was pressed (5 tons, disk of diameter 8 mm)
15 into a self-supporting pellet. Mounted onto a sapphire sample holder, the pellet was inserted in
16 the reaction and XPS measurement cell, in which mixtures of $O_2/C_3H_8/He$ and $O_2/C_3H_8/H_2O_{(g)}$
17 with volume flows of 2 sccm/0.5 sccm/1.7 sccm were introduced via calibrated Bronkhorst mass
18 flow controllers. A constant total pressure of 25 Pa was established by a pressure regulating
19 valve. The overall gas phase composition was monitored by online mass spectrometry and,
20 furthermore, a proton transfer reaction mass spectrometer (PTR-MS, IONICON) was used to
21 determine the abundance of acrylic acid. Heating of the pellet was realized from the sample back
22 using an NIR laser, whose power was adjusted through a PID feedback loop controlled by a K-
23 type thermocouple in contact with the sample surface. The heating rate was 5 K/min up to a final
24 temperature of 270°C. Core level spectra of O 1s, V 2p, Mo 3d, and C 1s were collected at
25 constant kinetic energies of the photoelectrons of 150 eV and 750 eV, resulting in inelastic mean
26 free paths (IMFP) of ~0.6 nm and ~1.6 nm, respectively, according to the model of Tanuma *et*
27 *al.*²⁵ The XPS spectra were normalized by the storage ring current and the photon energy
28 dependent incident photon flux. The binding energy (BE) scale was calibrated with respect to the
29 valence band onset. V 2p_{3/2} peak deconvolution and quantitative element abundance calculations
30
31
32
33
34
35
36
37
38
39
40
41
42
43
44
45
46
47
48
49
50
51
52
53
54
55
56
57
58
59
60

1
2
3 were performed with the commercially available CASA XPS data analysis software (Neil Farley,
4 www.casaxps.com) after subtracting a Shirley-type background and by taking into account the
5
6 photon energy dependent photo-ionization cross sections.²⁶ The error bar of the absolute
7
8 elemental composition can be estimated up to 20 % due to uncertainties in the monochromatic
9
10 photon flux, cross sections, and peak areas. However, only the uncertainty in peak area
11
12 determination contributes to relative uncertainties in an experimental series. Therefore, the
13
14 relative error bar in the XPS figures can be estimated to be ~2 %.

21 RESULTS AND DISCUSSION

25 1. Structural Characterization of the Catalyst

26
27 X-ray powder diffraction (Fig. S2a) and SEM images (Fig. S3) of (Mo,V)O_x reveal phase
28
29 purity and high crystallinity of the synthesized material. The particle size distribution is broad
30
31 and the shape of the particles not uniform. Very small particles are also observed (Fig. S3).
32
33 However, high-resolution electron microscopy of the small particles selected by transmission
34
35 electron microscopy reveal that also these particles are composed of the crystalline M1 phase
36
37 (Fig. S4). The bulk metal composition determined by EDX corresponds to 29.5 at% V and 70.5
38
39 at% Mo.

40
41
42
43
44 The bulk structure of individual oxide particles of (Mo,V)O_x was investigated by ABF-STEM
45
46 (Fig. 1). As opposed to the HAADF detector, the ABF detector allows to image light elements in
47
48 the vicinity of heavy atoms. The image resembles the complex nano-structural array of metal
49
50 cations typical for orthorhombic (Mo,V)O_x. In addition, the images display a partial occupation
51
52 of hexagonal and heptagonal channels for these complex metal oxides (indicated by the red
53
54 arrow), which cannot be observed using a HAADF detector (Fig. S5).

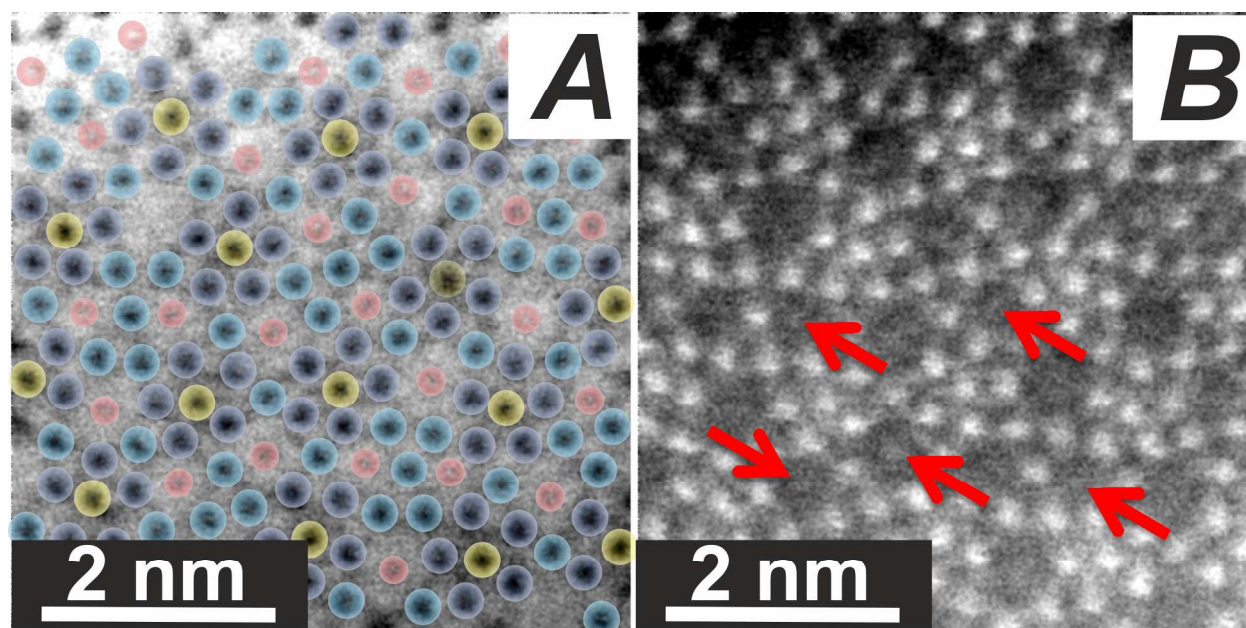


Figure 1. Imaging the nanostructure of the M1 phase viewed along [001]. (A) Atomic resolution ABF-STEM image of (Mo,V)O_x; With the help of the color the various polyhedrons and channel sites can be distinguished; The color corresponds to the color of the polyhedrons used in Figure 2 (pentagonal bi-pyramidal unit in yellow, octahedrons surrounding the pentagonal unit in dark blue, linking octahedrons in light blue, and channel sites in red); In order to highlight the occupation of the channel sites the inverted ABF-image is shown in (B) (red arrows indicates occupation); The original image is presented in Fig. S6.

The size of some crystallites in the polycrystalline (Mo,V)O_x allowed a synchrotron X-ray single crystal analysis. A summary of the crystallographic data is given in Table 1, and Tabs. S1-S2. The structural details of the orthorhombic M1 phase were first elucidated for the (Mo,V,Te,Nb)O_x system by combined Rietveld refinement of synchrotron X-ray and neutron powder diffraction data.²⁷ Later, (Mo,V,Sb)O_x was the first M1 type structure to be characterized by synchrotron-based single crystal analysis.²¹ Generally speaking, M1 belongs to the family of molybdenum bronzes, which have a ca. 4 Å crystallographic axis in common. This distance represents the length of two M–O bonds forming the backbone of linear chains of corner-sharing polyhedra in this direction.

1
2
3
4
5
6
7
8 **Table 1. Crystallographic data for (Mo,V)O_x**
9

10		
11	Formula	Mo _{7.88} V _{2.61} O _{29.25}
12	M (g mol ⁻¹)	1356.76
13	T (K)	100(2)
14	λ (Å)	0.85507
15	crystal system	Orthorhombic
16	space group	<i>Pba2</i> (No. 32)
17	a (Å)	21.0590(7)
18	b (Å)	26.5310(8)
19	c (Å)	3.9810(10)
20	V (Å ³)	2224.2(6)
21	Z	4
22	ρ_{calcd} (g cm ⁻³)	4.052
23	μ (mm ⁻¹)	8.435
24	F_{000}	2500
25	measured reflections	31034
26	independent reflections	5381 ($R_{\text{int}} = 0.0485$)
27	data / restraints / parameters	5381 / 1 / 232
28	goodness of fit	1.061
29	R_1 ($I > 2\sigma(I)$)	0.0474
30	wR_2 (all data)	0.1206
31	Flack parameter	0.045(16)
32	extinction coefficient	0.00182(19)
33	largest diff. peak / hole (e Å ⁻³)	4.617 / -2.091
34		
35		
36		
37		
38		
39		
40		
41		
42		
43		
44		
45		
46		
47		
48		
49		
50		
51		
52		
53		
54		
55		
56		
57		
58		
59		
60		

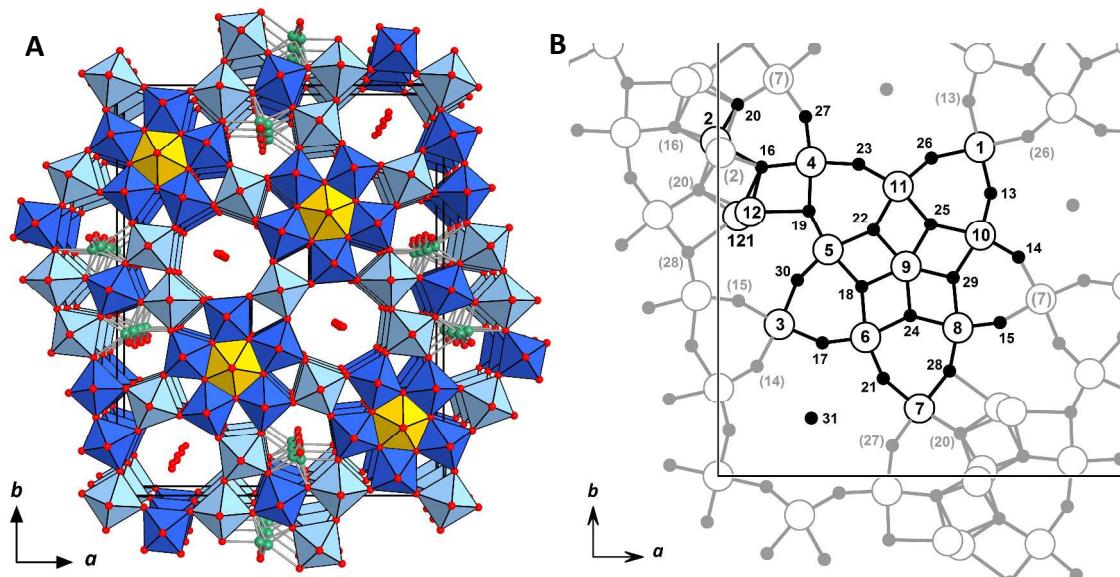


Figure 2. Polyhedral representation of the M1 structure (A), and asymmetric unit of the (Mo,V)O_x M1 crystal structure with atom numbering scheme (B); Axial oxygen atoms are numbered like the corresponding metal atoms and have been omitted for clarity.

One prominent feature of the M1 structure is the presence of a pentagonal building block (colored in yellow in Fig. 2 A). This unit consists of a MO₇ pentagonal bipyramid, which shares its equatorial edges with five MO₆ octahedra (colored in dark blue in Fig. 2 A). This structural motif is not only shared with a family of supramolecular polyoxometallate compounds,²⁸ but has also been shown to play a role as an actual building block during the M1 synthesis.^{21, 29-30} Furthermore, the same motif can be found in several related molybdenum bronze structures, most notably the Mo₅O₁₄ type.³¹ In both structures, the pentagonal motifs are linked by additional MO₆ octahedra (colored in light blue in Fig. 2 A) via corner sharing in equatorial plane, i.e. the plane perpendicular to the 4 Å *c* axis. In contrast to Mo₅O₁₄, which is more densely packed, the linkage in the M1 structure involves 6- and 7-membered rings, forming channels along the *c* axis (Fig. 2). These channels, of which the 7-membered ones can act as micropores,³² may contain a variety of statistically occupied species, such as water molecules or further metal atoms (indicated in red in Fig. 2 A).

1
2
3 For the crystal structure analysis presented here, the atom numbering scheme used by DeSanto
4 *et al.*⁹ and most subsequent authors was adopted (Fig. 2B). The general structural characteristics
5 agree well with the previously published studies. Inside the oxygen polyhedra, the metal atoms
6 exhibit a pronounced trend for off-center distortion, which is especially prominent along the *c*
7 axis of the M1 structure, resulting in alternating longer and shorter M–O distances in this
8 direction. In conjunction with the tendency of neighboring metal centers to avoid too short
9 metal-metal distances, this leads to a characteristic alternating “up and down” pattern
10 (puckering) of metal atoms with respect to the average metal plane (Fig. 3). It should be noted
11 that in the (Mo,V,Sb)O_x system, extensive disorder with respect to this out-of-plane
12 displacement has been reported.²¹ For all framework metal sites, there were two alternative
13 positions above and below the average (“pseudo-mirror”) plane. This site splitting yielded
14 unequal occupation, i.e. there were majority and minority sites found in this disorder.
15 Furthermore, the refined distribution between the two alternative positions was generally similar
16 for all sites, hinting a possible correlation. When regarded separately, the majority sites exhibit
17 the same alternating displacement pattern, which is seen in all other studies. Thus, we tend to
18 believe that this effect could be better explained as being caused by unresolved twinning, rather
19 than a correlated disorder across all metal sites.
20
21
22
23
24
25
26
27
28
29
30
31
32
33
34
35
36
37
38
39
40
41
42
43
44
45
46
47
48
49
50
51
52
53
54
55
56
57
58
59
60

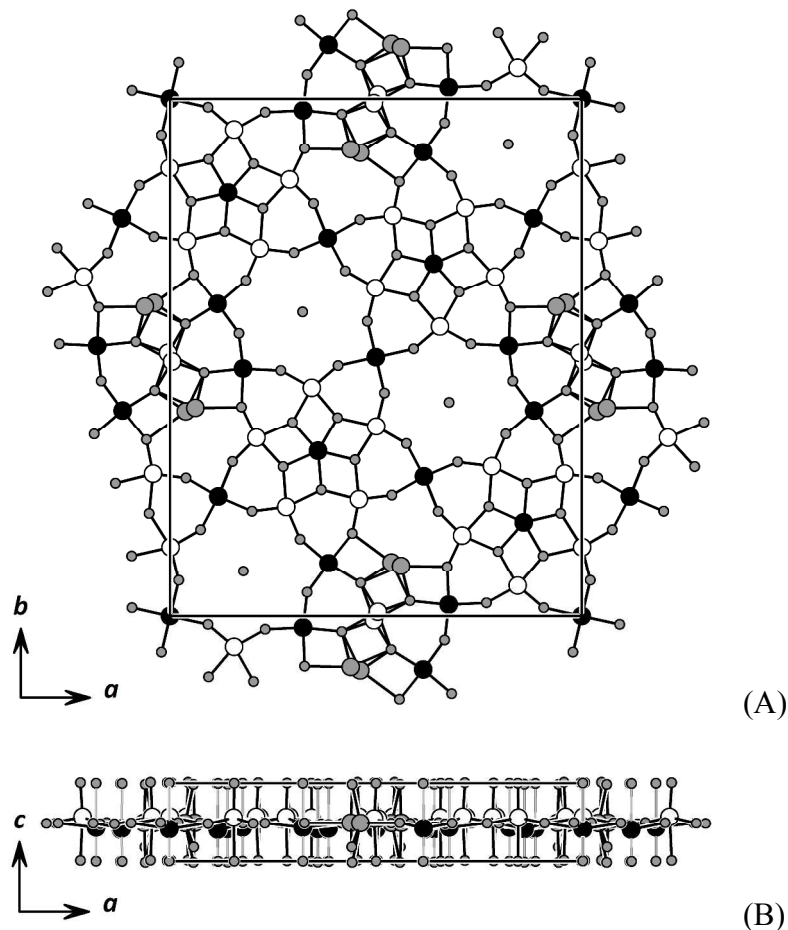


Figure 3. Out-of-plane displacement (puckering pattern) of metal sites in the M1 structure. (A) “Top” view onto the c -axis; only sites around the equatorial plane are shown, i.e. axial oxygen atoms have been omitted for clarity. (B) “Side” view along the b -axis. Atoms close to the $z = 0$ and $z = 0.5$ planes are shown in gray, while significant displacements of metal centers from the average plane are indicated in white ($z = 0.5 + \delta$) and black ($z = 0.5 - \delta$), respectively.

Concerning the distribution of Mo and V on the various metal sites (for atomic numbering see Fig. 2B), our results are also consistent with the trends seen in previous reports: the sites belonging to the pentagonal unit (M9 and M5, M6, M8, M10, M11) are exclusively occupied by Mo, while most linker sites show a mixed Mo/V occupancy. Table 2 compares the metal distribution found in several studies.

Table 2. Comparison of metal distribution and resulting (i.e. diffraction derived) composition from several published M1 single crystal (SC) and Rietveld (R) structure analyses. For the framework sites M1-M11, the Mo occupancy is given, and the remainder of the site is filled with V unless noted otherwise. In contrast, the channel sites M12 and M13 are only partially occupied. For convenient comparison, the alternative site numbering scheme used by Ishikawa *et al.*³³ is added in parentheses

	SC ^{this work}	SC ³³	SC ²¹	R ³⁴	R ⁹	R ³⁵
Composition	Mo,V	Mo,V	Mo,V,Sb	Mo,V,Nb,Te	Mo,V,Nb,Te	Mo,V,Ta,Te
framework	79:21	76:24	81:19:0	73:17:10:0	78:12:10:0	82:14:4:0
total	75:25	76:24	77:18:5	68:16:9:6	71:11:9:9	75:13:4:8
M1 (M11)	0.26	0.11	0.32	0.46	0.74	1
M2 (M7)	1	0.75	0.84	0.63	0.38	0.37
M3 (M10)	0.24	0.24	0.39	0.46	0.58	0.34
M4 (M9)	0.55	0.62	0.53	0.88	1	1
M7 (M8)	0.45	0.33	0.60	0.62	0.68	0.59
M5 (M5)	1	1	1	0.8	1	1
M6 (M1)	1	1	1	1	1	1
M8 (M4)	1	1	1	1	1	1
M10 (M3)	1	1	1	1	1	1
M11 (M2)	1	1	1	1	1	1
M9 (M6)	1	1	1	0 / 1 Nb	0 / 1 Nb	0.56 / 0.44 Ta
M12 [hex.]	0.49 V	-	0.52 Sb	0.69 Te	0.74 Te	0.67 Te
M13 [hept.]	-	-	-	-	0.20 Te	0.18 Te

The sites M1 and M2 are special positions located on 2-fold rotational axes. M1 resides between two 7-membered rings and seems to have a tendency to be rich in V, with the exception of the (Mo,V,Te,Nb)O_x and (Mo,V,Te,Ta)O_x Rietveld studies of DeSanto *et al.*³⁵ Position M2 is located between two 6-membered rings and is mostly found to be rich in Mo. This M2 site shows some interesting characteristics, which, to our knowledge, have not been discussed in detail before. In our study, we observed a strongly anisotropic thermal displacement parameter, with its long axis pointing approximately to the centers of the 6-membered rings. In the recent single

1
2
3 crystal study of (Mo,V)O_x by Ishikawa *et al.*,³³ the same effect can be seen in the supporting CIF
4 data. For the final refinement, we decided to use an alternative model, describing M2 with an
5 isotropic thermal parameter, but liberating the atom position from the special position
6 restrictions, effectively splitting the site symmetrically around the twofold axis. The refined
7 position is displaced slightly towards the channel centers. While not explicitly discussed by
8 Sadakane *et al.*, an analogous splitting is depicted in the supporting material for the majority
9 component of the M2 site in MoVSbO_x.²¹ Thus, we believe that this out-of-axis displacement is a
10 general characteristic of the M1 structure. There are two factors, which can be made responsible
11 for this disorder around the symmetry element. First, molybdenum and vanadium in their d⁰ state
12 show different preferences concerning the mode of off-center distortion in an octahedral
13 environment. V⁵⁺ (and also V⁴⁺ to a slightly lesser extent) prefers a displacement towards one
14 ligand (the vanadyl oxygen atom), i.e. along an axis of the octahedron. Mo⁶⁺, on the other hand,
15 is usually displaced towards an octahedron edge between two neighboring ligand atoms.³⁶ For
16 the sites M1 and M2, the twofold rotational symmetry axis coincides with one axis of the
17 coordination octahedron. Thus, at the V-rich M1 site, the site symmetry and the preferred
18 vanadium distortion along the axis are compatible with each other. In contrast, this symmetry
19 cannot accommodate the preferred distortion geometry for the Mo-dominated M2 site, thus
20 resulting in statistical disorder of the metal atom around the rotation axis. The second factor
21 comes into play when the hexagonal channels contain additional metal atoms on the M12 site,
22 like, *e.g.*, Te or Sb. In our crystal structure analysis, we found significant electron density at the
23 M12 site, which was too close (around 2.0 ± 0.2 Å) to the nearest oxygen sites (O16, O20) to
24 represent a water oxygen or ammonium nitrogen atom. Since Mo and V are the only metals in
25 our sample, we interpret this electron density as a statistically occupied vanadium site. As partial
26
27
28
29
30
31
32
33
34
35
36
37
38
39
40
41
42
43
44
45
46
47
48
49
50
51
52
53
54
55
56
57
58
59
60

1
2
3 occupation seems to be a general feature of the M12 site, it is quite conceivable that this kind of
4
5 disorder will also affect the M2 site, to which is tightly connected via two common oxygen
6
7 atoms. In other words, we assume that the statistical disorder of the M12 site in the channels
8
9 enhances the already present out-of-axis distortion at the mostly Mo-based M2 site by metal-
10
11 metal repulsion. It should be noted that the published Rietveld analyses assign less Mo (more V)
12
13 to M2 than the single crystal studies. In the light of the evidence for M2 site splitting around the
14
15 twofold axis, one may argue that the Rietveld results could be biased in this respect. The splitting
16
17 would cause a dilution of electron density in the center, which may then be mistaken for a lower
18
19 average atomic number in an isotropic, symmetry restricted refinement model.
20
21
22
23

24 The origin of the vanadium atoms in the hexagonal channels is not completely clear. For
25
26 comparison, we also investigated a crystal of the washed sample before thermal activation, and
27
28 found no significant electron density at the M12 site. Furthermore, the anisotropy (or splitting,
29
30 depending on the model used) of the associated M2 site was clearly less pronounced than in the
31
32 activated sample. Thus, the vanadium atoms must have migrated onto the M12 site during the
33
34 thermal activation treatment. There are two possibilities for the origin of this extra-framework
35
36 vanadium: either, it came from the surrounding framework sites, leaving some cation vacancies
37
38 there, or it migrated into and along the channels from the outside (surface/amorphous material).
39
40 Considering the behavior of M1-type catalysts under changing environmental conditions,²⁰ the
41
42 migration hypothesis seems more likely. A direct crystallographic test by including framework
43
44 vacancies in the refinement model is, however, not possible. Dropping the boundary condition
45
46 that the Mo and V occupations of regular sites must add up to unity would leave the refinement
47
48 model mathematically underdetermined.
49
50
51
52
53
54
55
56
57
58
59
60

1
2
3
4
5
6
7
8
9
10
11
12
13
14
15
16
17
18
19
20
21
22
23
24
25
26
27
28
29
30
31
32
33
34
35
36
37
38
39
40
41
42
43
44
45
46
47
48
49
50
51
52
53
54
55
56
57
58
59
60

Inside the heptagonal channels, only low electron density was found. Judging from the ca. 3 Å distance to the nearest oxygen atoms, these species can be interpreted as partially occupied water molecules or residual ammonium ions. Specifically, the M13 site of DeSanto *et al.*⁹ was found to be empty. This result is in line with a certain microporosity of the MoV M1 oxide (Fig. 4). The external surface area of 9.8 m²/g can be differentiated from micropore surface area (18.1 m²/g) by the t-plot method.²² The total surface area as determined by the BET method corresponds to 27.9 m²/g. The calculated pore diameter of 5 Å perfectly reflects the structural heptagonal pores of the M1 phase. Accordingly, these pores are at least accessible for nitrogen. Adsorbed propane is characterized by cross-sectional area of > 30 Å in average meaning that the molecule may be adsorbed only at the pore mouth.³⁷

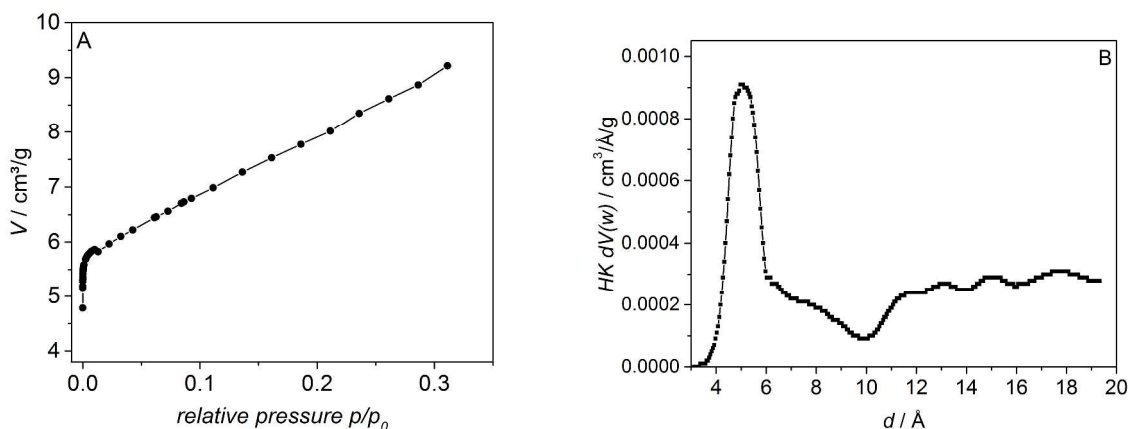


Figure 4. Adsorption isotherm of nitrogen at -196°C at low relative pressures used for micropore and surface area analysis (A), and pore size analysis of (Mo,V)O_x according to the Horvath-Kawazoe (HK) method (B).²²

2. Oxidation of Propane

Due to its low thermal stability, MoV M1 oxide cannot be measured in propane oxidation under the same reaction conditions as MoVTenb M1 oxide. The typical working temperature of MoVTenb M1 oxide in selective oxidation of propane to acrylic acid in an oxygen-rich feed

1
2
3 (O₂:C₃H₈=2) that contains 20-40 vol% steam is 350-420°C. Under such conditions the yield of
4
5 the most desired reaction product acrylic acid approaches 30-50% depending on the preparation
6
7 method of the solid that influences chemical composition, particle size, and morphology.¹⁸ The
8
9 lower thermal stability of MoV M1 oxide is reflected in catalyst deactivation at T>300°C due to
10
11 decomposition of the mixed oxide into its binary oxides. Therefore, MoV M1 oxide has been
12
13 studied in the temperature range between 250 and 300°C. At these temperatures the MoV M1
14
15 oxide bulk structure is stable (Fig. S2). No phase separation and only slight changes in the lattice
16
17 parameters have been observed after catalysis (see caption of Fig. S2 for lattice parameters). The
18
19 contact time has been chosen to adjust the propane conversion between 5 and 15 % (Fig. 5).
20
21 Undesired molecules CO, CO₂, and acetic acid are the major reaction products under these
22
23 conditions over MoV M1 oxide. Acetone is formed in lower amounts. Products of selective
24
25 reactions comprise propene (17-10%), and acrylic acid (15-10%). Most interestingly, the notable
26
27 amount of acrylic acid formed over MoV M1 oxide reveals that the presence of tellurium in the
28
29 catalyst is not necessarily required for oxygen insertion reactions. The experiment does,
30
31 however, not exclude that Te may facilitate acrylic acid formation.^{17, 38} Water has an impact on
32
33 the selectivity to propene, which increases slightly by decreasing the steam content from 40% to
34
35 20% (compare Fig. 5 and Fig. S7) at the expense of acetic acid and carbon oxides. The
36
37 selectivity to acrylic acid is not very much affected in this range of steam concentrations (Fig. 5
38
39 and Fig. S7). The selectivity to acetone and propene decrease with increasing conversion in favor
40
41 of acrylic acid formation (Fig. 5). For comparison, conversion and product distribution in
42
43 propane oxidation over MoVTeNb M1 oxide at the usually applied reaction temperatures (380-
44
45 420°C) and low reaction temperatures (250-300°C) are shown in Figs. S7-8. The temperature
46
47 may have an impact on the solid-state kinetics of the catalyst with implications in terms of
48
49
50
51
52
53
54
55
56
57
58
59
60

oxygen activation and the abundance of differently reactive oxygen species on the catalyst surface. An increased concentration of electrophilic oxygen species at lower temperatures should be reflected in the product distribution. MoVTeNb M1 oxide is less active than MoV M1 oxide at low temperature (Fig. S7), but the products seem to follow roughly the same S-X curves at low and at high temperatures. This indicates that the reaction mechanism is not significantly changed due to the difference in the reaction temperature. The diversity of oxygenates is higher over MoV M1 oxide (Fig. S8). The trends in selectivity with increasing conversion (Fig. 5) suggest that lower selectivity towards acrylic acid over MoV M1 oxide compared to MoVTeNb M1 oxide is a result of post-combustion of formed selective oxidation products.

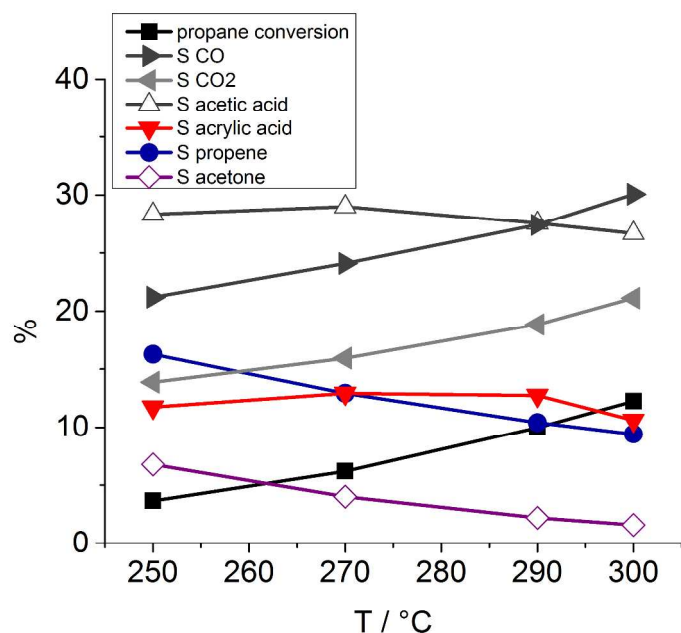


Figure 5. Conversion of propane and product distribution over $(\text{Mo},\text{V})\text{O}_x$ as a function of temperature; Feed composition: 3% C_3H_8 , 6% O_2 , 71% N_2 , and 40% H_2O ; Contact time: 0.36 g s ml^{-1} .

This is also confirmed by an experiment in which the stability of acrylic acid over the catalyst at reaction temperature was tested. The acrylic acid is largely decomposed to acetic acid, CO, and CO_2 (Fig. S9).

3. Surface Dynamics of (Mo,V)O_x

The surface composition of vanadium and molybdenum has been monitored by NAP-XPS under operation of the catalyst at a reaction temperature of 270°C and a total pressure of 25 Pa. Fig. 6 A shows the normalized vanadium content with time on stream in alternating dry and wet feed (as indicated in the figure by steam ON and OFF) in surface sensitive measurement mode that comprises an inelastic mean free path of 0.6 nm according to the model of Tanuma *et al.*²⁵ The initial surface composition of MoV M1 oxide is in good agreement with the bulk composition of V:Mo=29.5:70.5 at%. The majority of V atoms are present in oxidation state 4+, but almost one quarter of the surface vanadium atoms occurs in the highest oxidation state. Alternative wet and dry feed causes the appearance and disappearance of acrylic acid, respectively, as monitored by proton transfer reaction mass spectrometry (black curve in Fig. 6 A). The surface composition does not follow these changes. Instead, a substantial increase in the total surface vanadium concentration up to more than 50 at% is noticed (brown curve in Fig. 6 A) with increasing time on stream that goes along with a progressive deactivation of the catalyst in terms of acrylic acid formation. The catalytic results presented for the plug flow reactor in Fig. 5 have been obtained under steady conditions, but changes in the selectivity to acrylic acid can also be observed under normal conditions by consulting the time on stream behavior. The selectivity to acrylic acid decreases within the first 30 minutes after reaching the reaction temperature, however only in wet feed (Figs. S10-11). At the same time, the conversion of propane increases slightly. The observations are in agreement with an enrichment of V⁵⁺ on the surface of the catalyst in wet feed as observed by NAP-XPS. The deceleration of the acrylic acid

decay in the XPS cell is attributed to the low total pressure, which may result in different solid-states kinetics, and differences in the flow conditions.

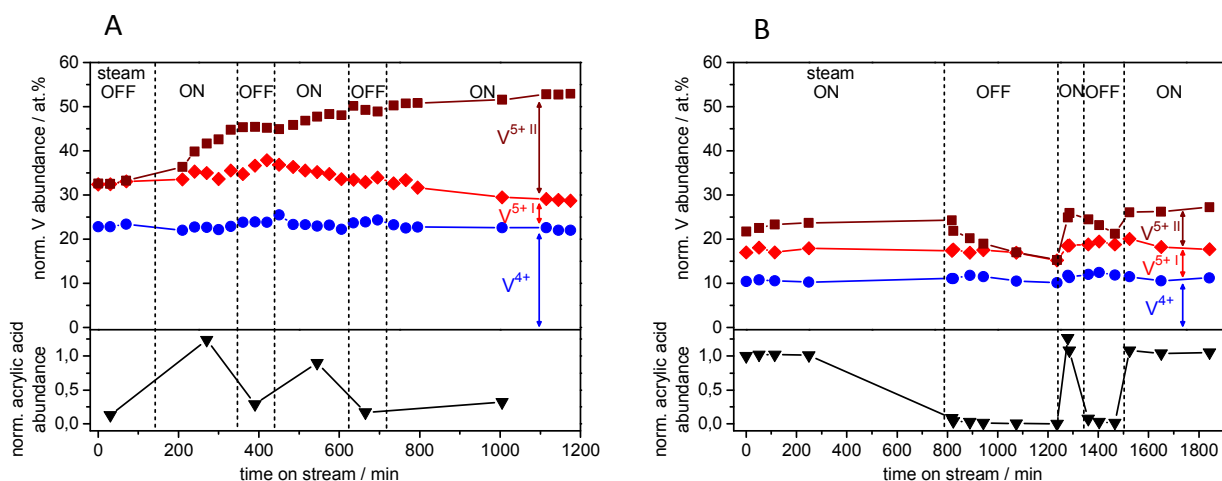
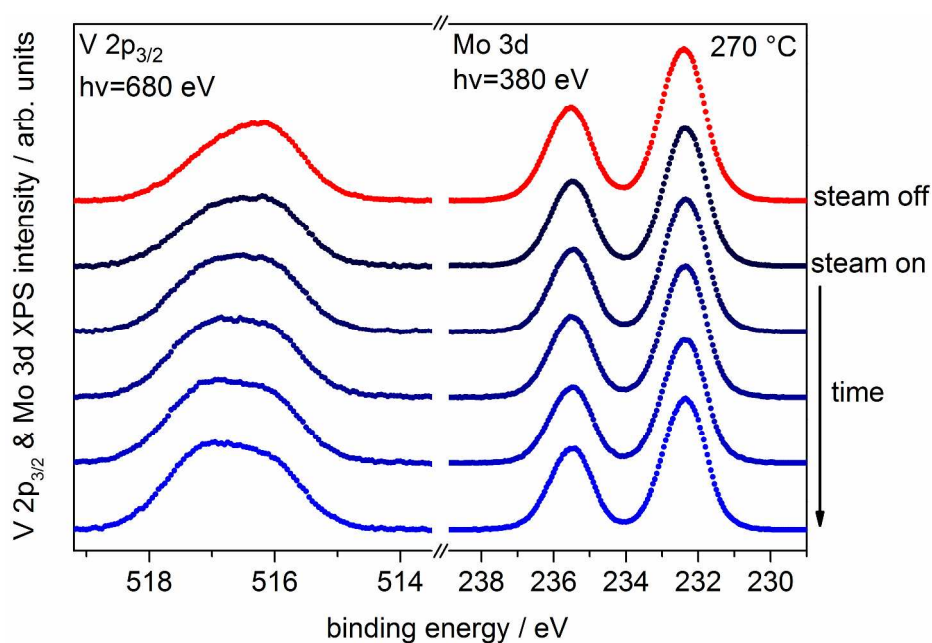


Figure 6. Normalized abundance of different V species at the surface (0.6 nm IMFP) of (Mo,V)O_x (A), and re-analyzed data of (Mo,V,Te,Nb)O_x published previously²⁰ (B) measured by XPS in presence of flowing mixtures of O₂/C₃H₈/He (steam OFF) and O₂/C₃H₈/H₂O_(g) (steam ON), respectively, (volume flows of 2 sccm/0.5 sccm/1.7 sccm) at T=270°C (A) and T=400°C (B), respectively, and a total pressure of 25 Pa; The V content is given in at% with respect to the sum of metals at the surface; The values are represented in an accumulative way: The blue curve corresponds to the surface concentration of V⁴⁺, the red curve corresponds to the sum of the surface concentration of V⁴⁺ and V⁵⁺(I), and the brown curve accounts for the overall surface concentration of V composed of the sum of V⁴⁺, V⁵⁺(I) and V⁵⁺(II) (for assignment see text); The black curve shows the acrylic acid abundance.

The changes in the peak profile of the V 2p_{3/2} peak shape with time after switching for the first time from dry to wet feed are depicted in Fig. 7 (left). The V 2p_{3/2} peak is initially centered at approximately 516 eV in dry feed with a small shoulder at higher binding energy (BE) around 517 eV. The shoulder got immediately more pronounced when switching to wet feed and steadily increased in its intensity with time in wet feed, which indicates progressive oxidation of vanadium from 4+ to 5+.³⁹⁻⁴⁰ The Mo 3d_{5/2} and Mo 3d_{3/2} peaks at 232.4 and 235.6 eV,

1
2
3 respectively, (Fig. 7, right) indicate that Mo exists essentially in oxidation state 6+,⁴¹ but small
4 contributions of molybdenum 5+ cannot be excluded.¹⁸ The oxidation state of molybdenum at
5 the surface remains constant under all reaction conditions. The asymmetry in the V 2p_{3/2} peak
6 develops progressively with time on stream in alternating wet and dry feed (Fig. 8, left). Again,
7 no change is observed concerning the state of molybdenum (Fig. 8, right).
8
9
10
11
12
13
14
15
16
17
18
19



41
42
43
44
45
46
47
48
49
50
51
52
53
54
55
56
57
58
59
60

Figure 7. Changes in the profile of V 2p_{3/2} (left), and Mo 3d (right) signals of (Mo,V)O_x with time after first time switching from dry (red spectra) to wet feed (blue spectra) (140 min – 330 min time on stream in Fig. 6) ; For reaction conditions see caption of Fig. 6.

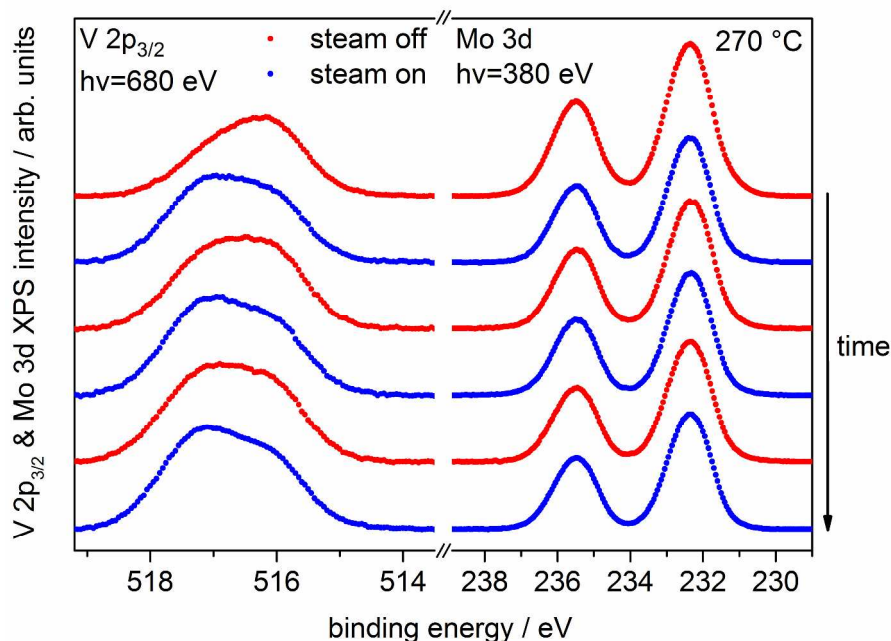


Figure 8. Long term changes (0 min – 1200 min time on stream in the experiment shown in Fig. 6) in the profile of the V $2p_{3/2}$ (left) and the Mo 3d signal (right) for $(\text{Mo},\text{V})\text{O}_x$ during switching from dry (red spectra) to wet (blue spectra) feed; For reaction conditions see caption of Fig. 6.

X-ray absorption spectroscopy (XAS) at the V $L_{3,2}$ edges has been applied to get additional information about the vanadium oxidation state and vanadium content at the surface. The overall energy position of the V L-edges at around 518eV (V L_3 -edge) and 524.6eV (V L_2 -edge) is a probe of the vanadium oxidation state.⁴² The shift to higher photon energies as it is observed in the course of the experiment with the $(\text{Mo},\text{V})\text{O}_x$ catalyst indicates a steadily increasing vanadium valence in agreement with the XPS V2p core level measurements (Fig. 7). While bound-bound V2p \rightarrow V3d transitions result in resonance structures at the V L absorption edges, continuum transitions become visible as a step-like intensity increase (“edge jump”). The edge jump is proportional to the number of absorbers, i.e. to the V content in the material. The edge jump intensity at the V L-edges at about 521 eV and 528 eV increases while the catalyst is exposed to different conditions with the most striking effect observed when dosing water vapor to the feed,

as it becomes obvious in Fig. 9. Hence, XAS confirms both the increase of vanadium oxidation state and the enrichment of vanadium on the surface of MoV M1 oxide during the experiment.

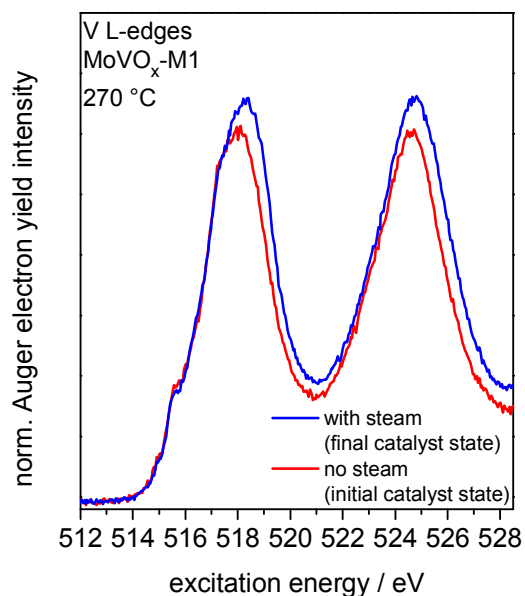


Figure 9. V $L_{3,2}$ -near edge X-ray absorption fine structure of $(\text{Mo},\text{V})\text{O}_x$ measured in presence of flowing mixtures of $\text{O}_2/\text{C}_3\text{H}_8/\text{He}$ and $\text{O}_2/\text{C}_3\text{H}_8/\text{H}_2\text{O}(\text{g})$, respectively, (volume flows of 2 sccm/0.5 sccm/1.7 sccm) at $T=250^\circ\text{C}$.

The peak profile of the V $2p_{3/2}$ signal has been analyzed for all data points applying a consistent constrained fit model to describe the variation in the data with high accuracy. An example of a fit of the V $2p_{3/2}$ core level of $(\text{Mo},\text{VO})_x$ is shown in Fig. 10 and a summary of the fit parameters can be found in Tab. S3. A fully constrained fit requires introduction of 3 fit profiles with binding energies of 516.1, 517.1, and 517.3 eV, respectively. The peak at 516.1 eV binding energy can readily be assigned to V^{4+} species while a BE of about 517 eV and higher suggests the presence of V^{5+} components, in good agreement with the literature⁴⁰ and references therein. A smaller FWHM is characteristic for V^{5+} components, e.g. in binary vanadium oxides.⁴⁰

Consequently, the slightly smaller FWHM of the fit profiles at BE 517 eV of about 1.25 eV-1.35 eV compared to the FWHM of 1.4 eV-1.45 eV found for the species at a binding energy of 516.1 eV supports the assignment to V^{5+} and V^{4+} species, respectively.

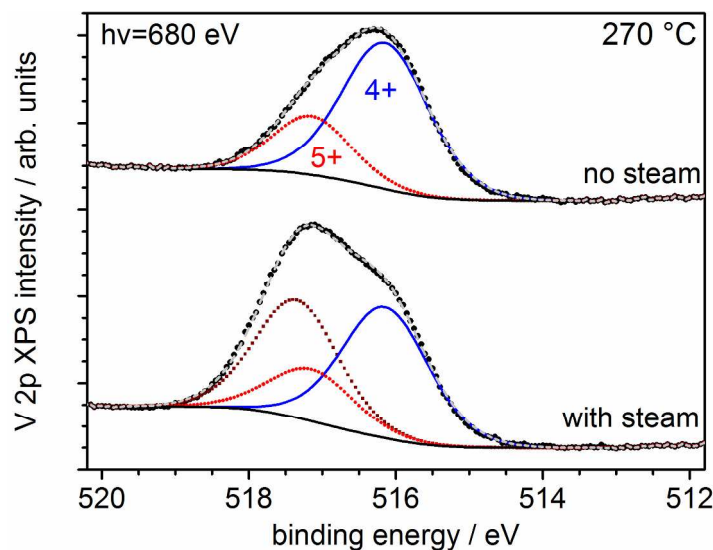


Figure 10. Least square fit of V $2p_{3/2}$ XP core level spectra of $(Mo,V)O_x$ without and with steam in the feed. Black dots represent the experimental data, blue, red, and brown dots vanadium 4+, 5+ (I), and 5+ (II) species, respectively. Grey dots are the sum of fit profiles and a Shirley background.

Literature values for BE of vanadium 2p core level lines vary considerably and make an assignment based just on the binding energy challenging.⁴³ Typically, no pronounced impact of the local geometric arrangement around the vanadium atom on the V2p BE has been found. Mekki *et al.* studied vanadium tellurite glasses and report only a very weak trend in BE shifts with Te/V ratio.⁴⁴ However, final state effects can significantly alter the BE of dispersed V^{5+} species.⁴⁵⁻⁴⁶ BE values of up to 518.7 eV have been reported for V^{5+} species. The inclusion of a 2nd V^{5+} species into the fit of the spectrum in steam (Fig. 10, bottom) is justified not only because of the improvement of the fit quality but also because the variation in the data can be described much more accurately. Furthermore, a function can be assigned to this additional V^{5+} (II) species

1
2
3 by comparison with the simultaneously obtained catalytic performance over MoV (Fig. 6 A) and
4 MoVTeNb (Fig. 6B) M1 oxide. For the purpose of comparison of the selective MoVTeNb M1
5 oxide with the rather unselective MoV M1 oxide, the data of MoVTeNb M1 oxide published
6 previously²⁰ have been re-analyzed applying the same fit procedure (Fig. 6B). The results
7 elucidate the full power of in-situ spectroscopies. Both catalysts show a rather constant amount
8 of V^{4+} that is not affected by dosing of steam while the V^{5+} (II) species with a BE of 517.3 eV is
9 created in the presence of steam in the feed. On (Mo,V)O_x the V^{5+} (II) species remains on the
10 surface also in dry feed to grow even more intense when steam is added to the feed in the next
11 cycle. In contrast, this vanadium 5+ (II) species is removed from the surface when MoVTeNbO_x
12 is treated in the same way, though at higher temperature. Also, the amount of V^{5+} (I) species
13 while steam is dosed remains rather constant during built up of V^{5+} (II) species in the case of the
14 (Mo,V,Te,Nb)O_x mixed oxide while the abundance of V^{5+} (I) species decreases steadily with the
15 continuous increase of V^{5+} (II) species for (Mo,V)O_x, but not by the same amount, though,
16 resulting in a slight increase in average vanadium oxidation state with time from 4.3 to 4.6 (Fig.
17 S12). The sum of V^{4+} and V^{5+} (I) based on the metal content is about 30 at% for MoV M1 oxide
18 and 17 at% for MoVTeNb M1 oxide, respectively. These numbers are in agreement with the
19 vanadium concentration in the bulk of MoV M1 oxide (29.5 at% as determined by EDX), and
20 MoVTeNb M1 oxide (18.8 at% as determined by X-ray fluorescence²⁰), respectively. This
21 suggests that V^{4+} and V^{5+} (I) species belong to the lattice of the oxide, while V^{5+} (II) is related to
22 extra-framework vanadium species.
23
24
25
26
27
28
29
30
31
32
33
34
35
36
37
38
39
40
41
42
43
44
45
46
47
48
49

50 The comparison of acrylic acid abundance and V^{5+} (II) intensity reveals that the (Mo,V)O_x
51 catalyst seems to deactivate with respect to acrylic acid formation due to the enrichment of
52 V^{5+} (II) species at the surface with time on stream (Fig. 6 A). In contrast, a correlation between
53
54
55
56
57
58
59
60

1
2
3 acrylic acid production and the overall V^{5+} abundance²⁰ was observed for MoVTeNb M1 oxide
4 (Fig. 6 B). In parallel to the accumulation of vanadium on the surface in wet feed, enrichment by
5 tellurium has been observed on MoVTeNb M1 oxide.²⁰ These surface dynamics have been
6 explained by hydrolysis of Te-O bonds within the channels of the M1 structure followed by
7 migration of Te hydroxide species to the outer surface. Since no deactivation of the MoVTeNb
8 oxide has been observed over very long times under varying feed conditions,²⁰ the formation of
9 vanadium tellurates at the surface has been postulated. Single crystal analysis of the $(Mo,V)O_x$
10 under study revealed partial occupation of metal position M12 in the hexagonal channels by
11 vanadium. In analogy to the MoVTeNb M1 oxide, the $V^{5+}(II)$ species might be associated with
12 vanadium oxide species that migrated from position M12 to the surface of the MoV M1 oxide
13 under reaction conditions due to hydrolysis of V-O bonds in the channels of the bulk oxide.
14 Increasing amount of such vanadium oxide species with V in the highest oxidation state leads to
15 decreasing selectivity towards acrylic acid as observed in the NAP-XPS experiment (Fig. 6 A).
16 Hydrolysis and migration to the surface seem to occur faster in case of MoVTeNb M1 oxide
17 perhaps due to the difference in temperature. In the experiment reported previously,²⁰ the
18 standard reaction temperature of 400°C has been applied for the thermally more stable
19 MoVTeNb M1 oxide. Furthermore, improved reversibility of this redox process is observed for
20 MoVTeNb M1 oxide (Fig. 6 B) compared to MoV M1 oxide (Fig. 6 A).
21
22
23
24
25
26
27
28
29
30
31
32
33
34
35
36
37
38
39
40
41
42
43
44
45
46
47
48

49 SUMMARY AND CONCLUSIONS

50
51
52 Highly crystalline mixed molybdenum-vanadium oxide composed of the M1 crystal structure
53 has been prepared by hydrothermal synthesis. Single crystal analysis of one particle of the
54 polycrystalline powder revealed that
55
56
57
58
59
60

- The central atoms of the pentagonal unit $M\{M\}_5$ are exclusively occupied by Mo;
- Most linker sites exhibit mixed Mo/V occupancy;
- The M12 site located in the hexagonal channels is statistically occupied by vanadium;
- The incorporation of V at the M12 sites occurs during thermal pretreatment of the catalyst at 400°C in Ar.

The MoV M1 oxide has been studied in oxidation of propane in a temperature range where the crystal structure is stable (250-300°C). Acrylic acid is also formed over the Te-free M1 structure in significant amounts implying that Te is not necessarily required as a component of the active ensemble responsible for selective oxygen insertion. As outlined above, tellurium is generally considered to be an indispensable constituent of the active ensemble on the catalyst surface involved in either consecutive selective oxidation of the intermediate propene to acrylic acid,¹² or in the activation of propane.¹⁷

Under working conditions, the (Mo,V)O_x surface is reconstructed and differs from the bulk in terms of composition and oxidation state of V. A substantial enrichment of V⁵⁺ species at the surface has been observed. Two electronically different V⁵⁺ species have been detected. The particular enrichment in one of these species (V⁵⁺(II), BE=517.3 eV) is attributed to the migration of vanadium from position M12 within the channels of the crystal structure to the surface under reaction conditions. The process is facilitated by hydrothermal conditions when the oxidation is carried out in presence of steam. Accumulation of vanadium in the highest oxidation state is detrimental in terms of acrylic acid formation. The very high surface concentration of more than 50 at% V might cause consecutive combustion of the desired reaction product acrylic acid. This assumption is based on the measured conversion-selectivity behavior of the catalyst. Detailed kinetic studies are in progress. The difference in selectivity of MoV and MoVTeNb M1

1
2
3 oxide is, therefore, attributed to differences in the dynamic site isolation that occurs differently
4
5 under reaction conditions at the surface of these two catalysts. The differences trace back to the
6
7 chemical composition of the bulk, in particular to the occupation of the M12 position in the
8
9 hexagonal channels on the one hand with vanadium in MoV M1 oxide and on the other hand
10
11 with (mainly) Te in MoVTeNb M1 oxide. The selective MoVTeNb M1 oxide features dynamic
12
13 site isolation due to segregation of Te serving as an uncritical diluent of surface V^{5+} oxide
14
15 species that are active in propane activation and oxygen insertion. The excessive enrichment of
16
17 V^{5+} at the surface of MoV M1 oxide promotes consecutive reactions of desired reaction
18
19 products. In addition, improved redox dynamics are achievable over MoVTeNb M1 oxide,¹⁹⁻²⁰
20
21 because the reaction can be performed at higher temperatures due to the higher thermal stability
22
23 of the latter catalyst compared to MoV M1 oxide.
24
25
26
27
28

29 The proposed site-isolation concept depicts the molecular pendant to our concept of band
30
31 bending,⁴⁷⁻⁴⁸ which is caused by segregation of an insulating or semiconducting 2-dimensional
32
33 surface layer that differs chemically from the bulk. The thin layer is formed in the feed of the
34
35 reactants as shown also in the present work for MoV M1 oxide. Composition as well as
36
37 oxidation state of the elements within the layer are influenced by the feed composition.⁴⁷ Band
38
39 bending controls the electron transfer between adsorbed species (reactants oxygen and alkane)
40
41 and the semiconducting solid and decouples oxygen reduction and hydrocarbon oxidation in
42
43 time. Underpinning the concept of site isolation,⁴⁹ we postulate at this point that both, electronic
44
45 and structural aspects are intrinsically tied to each other and need to be considered in the design
46
47 of selective oxidation catalysts. The detailed electronic properties of the MoV M1 oxide under
48
49 reaction conditions of alkane oxidation are currently under investigation.
50
51
52
53
54
55
56
57
58
59
60

Supporting Information. Atomic coordinates and displacement parameters of single-crystal analysis, XPS fit parameters, synthesis data, PXRD, SEM, TEM, catalytic data of propane oxidation and acrylic acid decomposition.

ACKNOWLEDGMENT

This work was conducted in the framework of the BasCat collaboration between BASF SE, TU Berlin, FHI, and the cluster of excellence “Unified Concepts in Catalysis” (UniCat www.unicat.tu-berlin.de). The authors thank Maike Hashagen and Jasmin Allan for technical assistance and Stephen Lohr for the preparation of MoV M1 oxide. We thank the HZB staff for their continual support of the electron spectroscopy activities of the FHI at BESSY II by providing beam time under proposal #14201159 and Dr. Christian Heine for his help in preliminary the NAP-XPS and NEXAFS measurements.

REFERENCES

1. Wachs, I. E.; Routray, K. *ACS Catal.* **2012**, *2*, 1235-1246.
2. Védrine, J. *Catalysts* **2016**, *6*, 22-48.
3. Licht, R. B.; Vogt, D.; Bell, A. T. *J. Catal.* **2016**, *339*, 228-241.
4. Deshlahra, P.; Carr, R. T.; Chai, S.-H.; Iglesia, E. *ACS Catal.* **2015**, *5*, 666-682.
5. Chieragato, A.; López Nieto, J. M.; Cavani, F. *Coord. Chem. Rev.* **2015**, *301-302*, 3-23.
6. Ishikawa, S.; Yi, X.; Murayama, T.; Ueda, W. *Catal. Today* **2014**, *238*, 35-40.
7. Schlögl, R. *Top. Catal.* **2011**, *54*, 627-638.
8. Man, I. C.; Su, H.-Y.; Calle-Vallejo, F.; Hansen, H. A.; Martínez, J. I.; Inoglu, N. G.; Kitchin, J.; Jaramillo, T. F.; Nørskov, J. K.; Rossmeisl, J. *ChemCatChem* **2011**, *3*, 1159-1165.
9. DeSanto, P., Jr.; Buttrey, D. J.; Grasselli, R. K.; Lugmair, C. G.; Volpe, A. F., Jr.; Toby, B. H.; Vogt, T. *Z. Kristallogr.* **2004**, *219*, 152-165.
10. Li, X.; Buttrey, D.; Blom, D.; Vogt, T. *Top. Catal.* **2011**, *54*, 614-626.
11. Celaya Sanfíz, A.; Hansen, T. W.; Sakthivel, A.; Trunschke, A.; Schlögl, R.; Knoester, A.; Brongersma, H. H.; Looi, M. H.; Hamid, S. B. A. *J. Catal.* **2008**, *258*, 35-43.
12. Grasselli, R. K.; Buttrey, D. J.; DeSanto, P.; Burrington, J. D.; Lugmair, C. G.; Volpe, A. F., Jr.; Weingand, T. *Catal. Today* **2004**, *91-92*, 251-258.
13. Shiju, N. R.; Liang, X.; Weimer, A. W.; Liang, C.; Dai, S.; Gulians, V. V. *J. Am. Chem. Soc.* **2008**, *130*, 5850-5851.

14. Ueda, W.; Vitry, D.; Katou, T. *Catal. Today* **2004**, *96*, 235-240.
15. Fu, G.; Xu, X.; Sautet, P. *Angew. Chem., Int. Ed.* **2012**, *51*, 12854-12858.
16. Naraschewski, F.; Jentys, A.; Lercher, J. *Top. Catal.* **2011**, *54*, 639-649.
17. Cheng, M.-J.; Goddard, W. A. *J. Am. Chem. Soc.* **2015**, *137*, 13224-13227.
18. Celaya Sanfiz, A.; Hansen, T. W.; Teschner, D.; Schnörch, P.; Girgsdies, F.; Trunschke, A.; Schlögl, R.; Looi, M. H.; Hamid, S. B. A. *J. Phys. Chem. C* **2010**, *114*, 1912-1921.
19. Hävecker, M.; Wrabetz, S.; Kröhnert, J.; Csepei, L.-I.; Naumann d'Alnoncourt, R.; Kolen'ko, Y. V.; Girgsdies, F.; Schlögl, R.; Trunschke, A. *J. Catal.* **2012**, *285*, 48-60.
20. Naumann D'Alnoncourt, R.; Csepei, L. I.; Hävecker, M.; Girgsdies, F.; Schuster, M. E.; Schlögl, R.; Trunschke, A. *J. Catal.* **2014**, *311*, 369-385.
21. Sadakane, M.; Yamagata, K.; Kodato, K.; Endo, K.; Toriumi, K.; Ozawa, Y.; Ozeki, T.; Nagai, T.; Matsui, Y.; Sakaguchi, N.; Pyrz, W. D.; Buttrey, D. J.; Blom, D. A.; Vogt, T.; Ueda, W. *Angew. Chem., Int. Ed.* **2009**, *48*, 3782-3786.
22. Lowell, S.; Shields, J. E.; Thomas, M. A.; Thommes, M., *Characterization of Porous Solids and Powders: Surface Area Pore Size and Density*. Kluwer Academic Publishers: Dordrecht, The Netherlands, 2004; p 129.
23. Naumann d'Alnoncourt, R.; Kolen'ko, Y. V.; Schlögl, R.; Trunschke, A. *Comb. Chem. High Throughput Screening* **2012**, *15*, 161-169.
24. Knop-Gericke, A.; Kleimenov, E.; Hävecker, M.; Blume, R.; Teschner, D.; Zafeirotos, S.; Schlögl, R.; Bukhtiyarov, V. I.; Kaichev, V. V.; Prosvirin, I. P.; Nizovskii, A. I.; Bluhm, H.; Barinov, A.; Dudin, P.; Kiskinova, M. In *Advances in Catalysis*, Bruce, C. G.; Helmut, K., Eds.; Academic Press: 2009; Vol. 52, pp 213-272.
25. Tanuma, S.; Powell, C. J.; Penn, D. R. *Surf. Interface Anal.* **1994**, *21*, 165-176.
26. Yeh, J. J.; Lindau, I. *At. Data Nucl. Data Tables* **1985**, *32*, 1-155.
27. DeSanto, P.; Buttrey, D. J.; Grasselli, R. K.; Lugmair, C. G.; Volpe, A. F.; Toby, B. H.; Vogt, T. *Top. Catal.* **2003**, *23*, 23-38.
28. Müller, A.; Kögerler, P.; Dress, A. W. M. *Coord. Chem. Rev.* **2001**, *222*, 193-218.
29. Canioni, R.; Marchal-Roch, C.; Leclerc-Laronze, N.; Haouas, M.; Taulelle, F.; Marrot, J.; Paul, S.; Lamonier, C.; Paul, J.-F.; Loridant, S.; Millet, J.-M. M.; Cadot, E. *Chem. Commun.* **2011**, *47*, 6413-6415.
30. Sanchez Sanchez, M.; Girgsdies, F.; Jastak, M.; Kube, P.; Schlögl, R.; Trunschke, A. *Angew. Chem. Int. Ed.* **2012**, *51*, 7194-7197.
31. Yamazoe, N.; Kihlberg, L. *Acta Crystallogr., Sect. B: Struct. Crystallogr. Cryst. Chem.* **1975**, *31*, 1666-1672.
32. Ishikawa, S.; Ueda, W. *Catal. Sci. Technol.* **2016**, *6*, 617-629.
33. Ishikawa, S.; Kobayashi, D.; Konya, T.; Ohmura, S.; Murayama, T.; Yasuda, N.; Sadakane, M.; Ueda, W. *J. Phys. Chem. C* **2015**, *119*, 7195-7206.
34. Murayama, H.; Vitry, D.; Ueda, W.; Fuchs, G.; Anne, M.; Dubois, J. L. *Appl. Catal., A* **2007**, *318*, 137-142.
35. DeSanto, P.; Buttrey, D.; Grasselli, R.; Pyrz, W.; Lugmair, C.; Volpe, A.; Vogt, T.; Toby, B. *Top. Catal.* **2006**, *38*, 31-40.
36. Ok, K. M.; Halasyamani, P. S.; Casanova, D.; Llunell, M.; Alemany, P.; Alvarez, S. *Chem. Mater.* **2006**, *18*, 3176-3183.
37. McClellan, A. L.; Harnsberger, H. F. *J. Colloid Interface Sci.* **1967**, *23*, 577-599.
38. Katou, T.; Vitry, D.; Ueda, W. *Chem. Lett.* **2003**, *32*, 1028-1029.

- 1
2
3 39. Sawatzky, G. A.; Post, D. *Phys. Rev. B: Condens. Matter Mater. Phys.* **1979**, *20*, 1546-
4 1555.
5
6 40. Biesinger, M. C.; Lau, L. W. M.; Gerson, A. R.; Smart, R. S. C. *Appl. Surf. Sci.* **2010**,
7 257, 887-898.
8 41. Brox, B.; Olefjord, I. *Surf. Interface Anal.* **1988**, *13*, 3-6.
9 42. Stöhr, J., *NEXAFS spectroscopy*. Springer: Berlin, New York, 1993.
10 43. Teschner, D.; Vass, E. M.; Schlögl, R. In *Metal Oxide Catalysis*, Wiley-VCH Verlag
11 GmbH & Co. KGaA: 2009; pp 243-298.
12 44. Mekki, A.; Khattak, G. D.; Wenger, L. E. *J. Electron Spectrosc. Relat. Phenom.* **2009**,
13 175, 21-26.
14 45. Wertheim, G. K. *Z. Phys. B: Condens. Matter* **1987**, *66*, 53-63.
15 46. Hess, C.; Tzolova-Muller, G.; Herbert, R. *J. Phys. Chem. C* **2007**, *111*, 9471-9479.
16 47. Heine, C.; Hävecker, M.; Sanchez-Sanchez, M.; Trunschke, A.; Schlögl, R.; Eichelbaum,
17 M. *J. Phys. Chem. C* **2013**, *117*, 26988-26997.
18 48. Eichelbaum, M.; Hävecker, M.; Heine, C.; Wernbacher, A. M.; Rosowski, F.; Trunschke,
19 A.; Schlögl, R. *Angew. Chem., Int. Ed.* **2015**, *54*, 2922-2926.
20 49. Grasselli, R. K. *Catal. Today* **2014**, *238*, 10-27.
21
22
23
24
25
26
27
28
29
30
31
32
33
34
35
36
37
38
39
40
41
42
43
44
45
46
47
48
49
50
51
52
53
54
55
56
57
58
59
60

